Experimental investigation of Bessel beam characteristics

Y. Lin, W. Seka, J. H. Eberly, H. Huang, and D. L. Brown

We report on an experimental characterization of Bessel beams with finite apertures. We show that real Bessel beams can be generated with intensity profiles that closely resemble the ideal J_o^2 transverse-intensity distribution of Bessel beams. We also show interferometrically that these beams have planar phase fronts with π-phase shifts from one Bessel ring to the next. We report tolerance conditions for Bessel beam generation and give an example of this generation that uses an unstable resonator as the light source.

Introduction

Some time ago Durnin[1] showed that the J_o Bessel function, as an exact solution to the free-space Helmholtz equation, may be of interest in optics. The particular interest in this solution lies in its diffraction-free propagation characteristics. That is, the J_o solution corresponds to the propagation of a narrow beam (i.e., the central portion of the J_o^2 transverse-intensity distribution) without transverse spreading over distances that can exceed by orders of magnitude the Rayleigh range of Gaussian beams of the same initial full width at half maximum (FWHM). In the ideal case, the electric field of the (zero-order) Bessel beam is given by

$$\mathbf{E}(r, \phi, z, t) = a \exp i(-\omega t + k_\parallel z) J_o(k_\perp r),$$

where the propagation direction is along z, $k_\parallel = (2\pi/\lambda)\cos\theta$, $k_\perp = (2\pi/\lambda)\sin\theta$, and θ is a fixed angle. However, one should not expect efficient power transport through Bessel beams, because the many side lobes accompanying the central spot contain most of the energy.[2–4]

Durnin *et al.*[2,4,5] have also reported some experimental verifications of these predictions. They used a thin metal ring mask that was illuminated by a He–Ne laser placed in the focal plane of a lens, as shown in Fig. 1, to generate a near-ideal Bessel beam. In particular, they showed a good agreement between the predicted and the experimentally measured longitudinal and transverse-intensity distributions.

An alternative experimental setup was reported by Turunen *et al.*,[6] who used a holographic optical element to generate the Bessel beam. These authors reported a 10% power conversion between the input power and the power contained in the Bessel beam. Although the cross-sectional intensity distribution closely resembles a J_o^2 beam, the central peak intensity varied rapidly with distance with a maximum toward the end of the useful focal range.

Two alternate schemes for generating long-focal-length beams have been suggested by Indebetouw.[7] One of these schemes uses a Fabry–Perot interferometer to generate a high-quality ring instead of Durnin's metallic ring mask, and the other one uses an axicon (a cone-shaped optical element) that is illuminated with a collimated beam. Although the former basically leads to the same results as Durnin's Bessel beam generator, the latter leads to increasing on-axis intensity with distance from the axicon caused by the increase in geometrical annular area contributing to the intensity on axis. This behavior is completely analogous to that in the setup of Turunen *et al.*[6]

Several authors[8] have attempted to implement various compromises between the features of Gaussian and Bessel beams. However, any such scheme necessarily limits the distance over which the central beam maintains its nondiffractive properties. Uehara and Kikuchi[9] have implemented a Bessel beam generator inside an Ar–ion laser cavity and have analyzed the results in terms of Bessel–Gauss beams with good success. Unfortunately, the resulting effective Bessel

The authors are with the Laboratory for Laser Energetics, 250 East River Road, Rochester, New York 14623-1299, and the Institute of Optics, University of Rochester, Rochester, New York 14627.

H. Huang is also with the Department of Physics and Astronomy, University of Rochester, Rochester, New York 14627.

Received 12 March 1991.

0003-6935/92/152708-06$05.00/0.

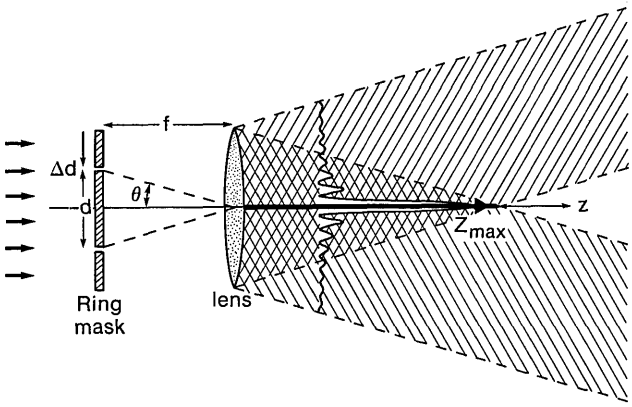

Fig. 1. Schematic setup for generating Bessel beams after Ref. 1.

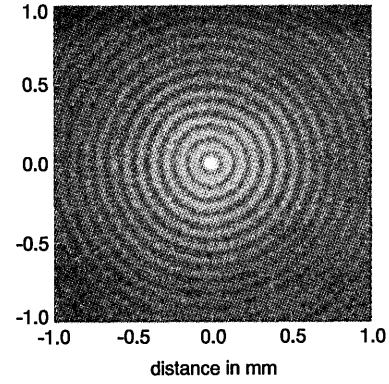

Fig. 2. Typical Bessel beam photograph obtained with a ring aperture of 12.1-mm diameter and 0.1-mm ring width, illuminated by a 1-ns, 1.054-μm, collimated laser pulse from a mode-locker ND:YLF laser. The photograph is taken at 1 m from the 1-m focal length lens (see Fig. 1).

beam propagation distance is only marginally longer than that of a Gaussian beam of the same FWHM, which diminishes the usefulness of this approach.

A recent calculational attempt by Thewes *et al.*[10] at converting a Gaussian beam into a Bessel beam with ~100% efficiency has ignored the π-phase jumps at each zero crossing of the Bessel beam. Thus, their double-aspheric lens could perhaps produce an intensity distribution at any single output plane that approximates a Bessel distribution; however, it will certainly not propagate like a Bessel beam.

Here we present experimental data at various laser wavelengths and pulse durations to point out some additional characteristics of finite-aperture Bessel beams beyond those that have been reported so far. In particular, we will show interferometric measurements of the phase front of Bessel beams, typical longitudinal and transverse-intensity distributions, and the extent to which they agree or disagree with predictions. We will also present detailed data on energy content in the Bessel rings. Finally, we will demonstrate that unstable resonators are potential efficient Bessel beam sources under certain conditions. The experimental results will be compared with the theoretical (i.e., ideal) Bessel beam predictions as well as with various computer simulations that use the actual experimental parameters, including the effects of phase-front distortions produced by the experimental setup.

Experimental Setup and Results

The Bessel beam generator setup shown in Fig. 1 was used for a number of experiments. Figure 2 shows a typical transverse Bessel beam profile using a 1.054-μm, Nd:YLF laser source of ~1-ns pulse duration. The annular ring mask was made from a metal-coated glass substrate into which a ring was etched that had a 12.1-mm inner diameter and a 0.1-mm ring width. The lens used to generate the Bessel beam was a 1-m focal length lens.

Bessel beam photographs were taken at several distances, out to 3.75 m, from the lens, well beyond the expected geometric focal range[1,5] for the Bessel beam of $Z_{max} \approx R/[\tan(d/2f)] \approx 2.8$ m. Here R is the smaller of either the radius of the lens or the effective radius of the diffraction pattern that is cast onto the lens. The effective radius is defined as $R_{eff} = d/2 + f\lambda/\Delta d$, where d and Δd are the diameter and width of the ring aperture, and f is the focal length of the lens. In the above case the focal range of our Bessel beam was limited by the size of the diffraction pattern on the lens, which was $R_{eff} \approx 17$ mm; the lens clear-aperture radius was 4 cm.

An azimuthal average about the center of symmetry of the Bessel beam in Fig. 2 is shown in Fig. 3. Also shown in Fig. 3 is a J_o^2 curve that is normalized to an average of the first six side lobes of the transverse-intensity distribution. This normalization was found to be the best one based on arguments that are presented later on in this paper. We note the generally good agreement between the experimental data and the ideal J_o^2 intensity distribution. The size of the central lobe, i.e., the diameter of the first zero ring (125 ± 5 μm), agrees well with the predictions ($d_{lz} = 4.81/k_\perp \approx 122$ μm). However, we also note that the central maximum is well below the expected value and that the minima in the distribution are not true zeros. This point will be discussed in more detail further down.

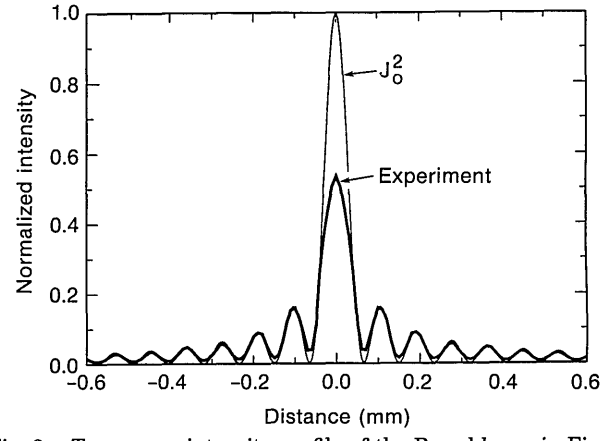

Fig. 3. Transverse intensity profile of the Bessel beam in Fig. 2 obtained from azimuthally averaging the digitized data Figs. 2 and 3.

From a series of images taken at different distances, we have obtained the longitudinal intensity distribution (Fig. 4) for the center lobe of the Bessel beam. Figure 4 also contains the simulated longitudinal intensity distribution based on numerical Fresnel diffraction simulations. The agreement between experiment and theory is again reasonable. The monotonically decreasing intensity distribution in Fig. 4 is a result of the finite lateral extent of the diffraction pattern from the mask that is cast onto a lens of larger dimensions. This distribution differs markedly from the longitudinal intensity distribution shown in Ref. 5 and reproduced in modified form in Fig. 5. In this case, the central beam intensity at long distances is determined primarily by the diffraction from the finite-lens aperture (lens-limited case, Fig. 5) and approaches that of an ideal Bessel beam (constant intensity) for a lens of infinite aperture and for an infinitely thin ring mask.

Figure 5 shows the on-axis Bessel beam intensities for the case in which the lens diameter equals the diameter of the ring mask ($2R_{\text{lens}} = d_{\text{ring}} = 12.1$ mm). The three distributions are for different ring widths. Figure 5(a) is typical for a lens-limited Bessel beam generated by a narrow ring width (25 μm), which casts a diffraction pattern onto the lens that far exceeds the lens dimensions. As the ring width is increased, the on-axis intensity distribution deviates more and more from ideal Bessel beam propagation [see Figs. 5(b) and (c)]. Figure 5 also shows the on-axis intensity distribution for a Gaussian beam whose initial FWHM at $z = 0$ equals that of the Bessel beam.

When comparing Figs. 4 and 5, we note that for a lens of given focal length the focal range of Bessel beams is always larger for the diffraction-limited case (Fig. 4) than for the lens-limited case (Fig. 5). However, in all cases the focal range of the Bessel beams significantly exceeds that of the Gaussian beams of initially equal FWHM.

A characteristic of Bessel beams is that each ring in the pattern carries approximately the same energy

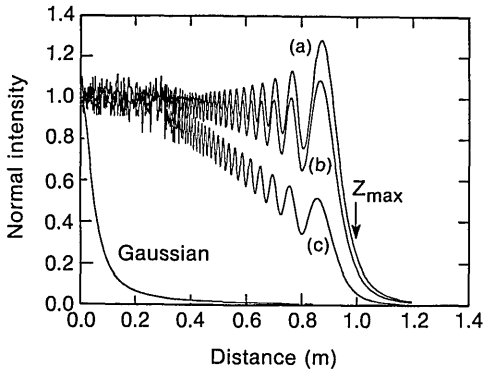

Fig. 5. Longitudinal intensity distribution of the central Bessel lobe for lens-limited Bessel beams with equal lens and ring diameters (12.1 mm) and ring widths of (a) 25 μm, (b) 50 μm, and (c) 100 μm. The focal length of the lens is $f = 1$ m at $\lambda = 1$ μm.

(or power). We have verified this prediction in Fig. 6 for the Bessel beam shown in Fig. 3. The numerical predictions for the ring energies for this particular experimental setup are practically identical to those made on the basis of J_o^2 and basically agree with the experimental data, except for a systematic trend in the center lobe intensity.

There are several potential sources for this apparent low center lobe intensity, such as film characteristics, phase-front distortions, mask-geometry distortions, and beam-phase or intensity modulation. The film D–log I response of the Kodak high-speed IR film was accounted for by calibration[11] under the actual experimental conditions. However, a preliminary examination of the modulation transfer function (MTF) of this film under our experimental conditions using a 100% modulated, variable frequency sine-wave interference pattern indicates that the MTF does not exceed a value of ~0.41. This limitation reduces the maximum achievable contrast, $(I_{\max} - I_{\min})/(I_{\max} + I_{\min})$, to <3 and thus is likely to be the major reason for the measured low central spike intensity.

The influence of phase distortions originating in

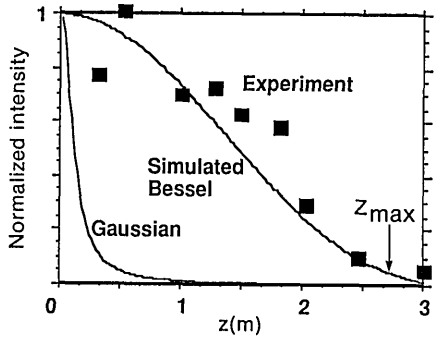

Fig. 4. Intensity distribution of the central Bessel lobe along the direction of propagation for the Bessel beam shown in Fig. 3. The intensity at large distances is determined primarily by the limited extent of the diffraction pattern of the ring mask rather than by the dimension of the lens. Also shown are the predicted intensity distribution based on Fresnel diffraction calculations and the longitudinal intensity distribution for a Gaussian beam of equal FWHM at the lens.

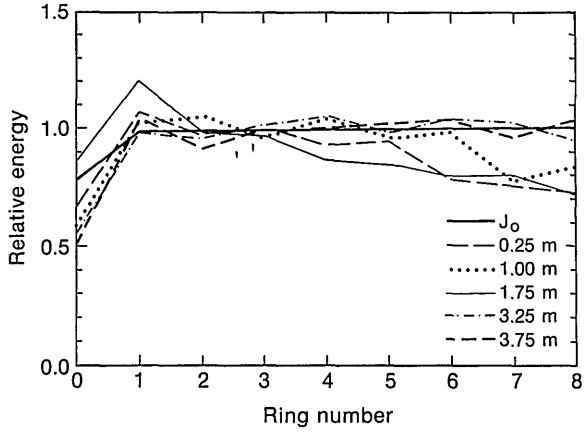

Fig. 6. Comparison of theoretical and experimental Bessel ring energies at various distances along the Bessel beam propagation. The Bessel beam is the same as that shown in Fig. 2. The systematic deficiency in the experimental energy content of the center lobe is primarily caused by limited film MTF.

the mask have been studied with a numerical far-field computer code that divides the near-field amplitude and phase distributions at the Bessel mask into small squares, whose far-field sinc-squared functions are then added with their respective amplitudes and phases.[12] This method guarantees high far-field resolution and is easily implemented on a small computer. Using the experimentally measured low-frequency phase distortion of the mask substrate [$\Delta\phi_{rms} \approx 0.075$ wave with ~ 0.3 wave peak to valley at $\lambda = 1$ μm; see Fig. 7(a)], we reduce the center peak intensity of the resulting Bessel beam only by $\sim 10\%$. Similarly, a high-frequency phase noise of $\leq \lambda/4$ rms and ~ 25-μm scale size originating in the Bessel mask reduces the intensity of the whole pattern by more than an order of magnitude, whereas the shape of the azimuthal average is almost identical to a perfect Bessel beam. The speckle pattern produced in this way has a typical scale size that is equal to or larger than the central spot size [see Fig. 7(b)]. This kind of speckle is easily identified experimentally and was absent in our experiments. The fine structure seen in Fig. 2 has been identified as film grain and is much too small to be produced by the lens shown in Fig. 1, even if it had been of poor quality. Note that the Strehl ratio[13] is not a good guide in this context, as it is applicable only to phase noise of $\Delta\phi_{rms} < (2\pi)^{-1}$ and gives no information concerning the intensity distribution in the far field.

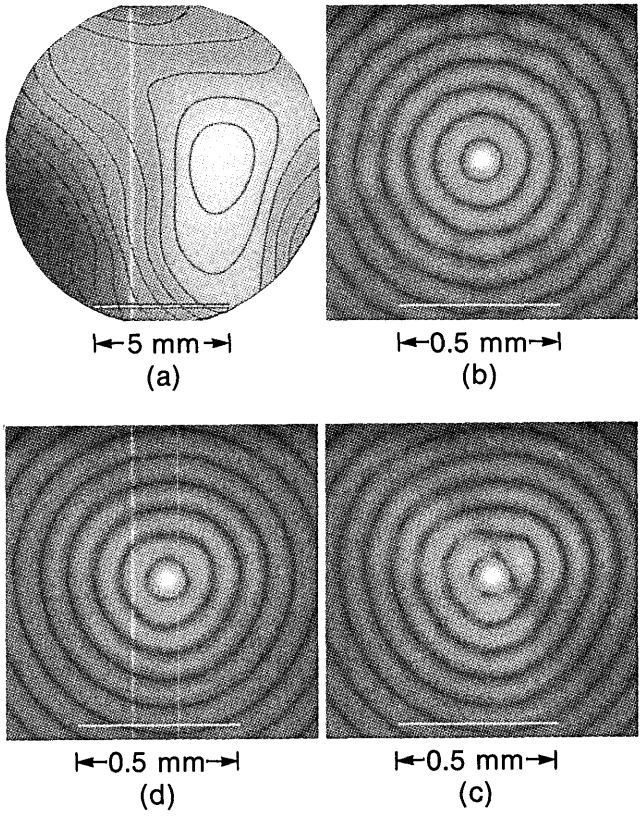

Fig. 7. Measured phase-front distortions ($\lambda/40$ contours at $\lambda = 1$ μm) of the Bessel ring substrate showing (a) three-lobed distortion (0.3 λ peak to valley at $\lambda = 1$ μm), probably caused by cutting of the substrate during fabrication; simulated far-field (b) intensity distribution for a ring mask with $\lambda/4$ rms high-frequency noise (~ 25 μm scale size), leading to clearly identifiable speckle structure in the rings outside the center lobe; (c) and (d) distributions of Bessel beams generated with the measured phase front shown in (a) and scaled for $\lambda = 1$ μm and 0.5 μm, respectively.

Effects caused by laser-beam quality in either phase or intensity distribution are easily checked by changing the mask position in the beam. We found that beam quality had no measurable influence on the measured intensity distributions, as we expected for our spatially filtered and collimated laser beams. Finally, imperfections in mask geometry are easily checked with the far-field code described above. Small deviations from perfect geometry, which may be caused by numerically generated masks, result in no measurable deviations from perfect Bessel beams, whereas systematic distortions such as oval rings or off-center inner disks insignificantly affect the center peak intensity while strongly affecting the circular symmetry of the innermost rings. In this regard, the effects of mask-geometry imperfections are similar to the low-frequency phase-front distortions. In summary, the low center lobe intensities in Figs. 3 and 6 are primarily attributable to film characteristics, with intensity and phase distortions playing only a minor role.

The low-intensity regions that should be true zeros for perfect Bessel beams are also explained by the poor MTF performance of the film. Unfortunately, high dynamic range measurements are notoriously difficult in the $\lambda \sim 1$ μm range and for pulsed operation, particularly if high spatial resolution is required. Beyond the first zero ring the measured azimuthally averaged intensity distributions (Fig. 3) match the perfect J_o^2 dependence quite well, as we would expect for the much lower dynamic range requirements in this region. This match was our rationale for normalizing the J_o^2 function to the wings of our measured intensity distributions.

To verify proper scaling of the Bessel beam properties as well as to facilitate identification of experimental limitations in producing Bessel beams, we have generated, with the same mask, Bessel beams at $\lambda_1 = 1.054$ μm (Nd:YLF, pulsed) and at $\lambda_2 = 0.51$ μm (Ar^+, cw), shown in Figs. 2 and 8, respectively. The 0.5-μm Bessel beam (Fig. 8) clearly shows a threefold

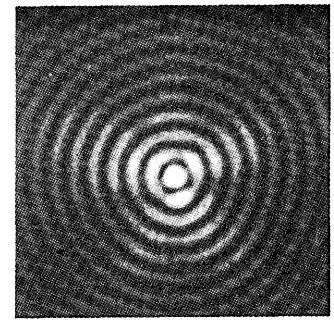

Fig. 8. Transverse intensity distribution of a Bessel beam generated with the same mask as used for Fig. 1 but at $\lambda = 0.51$ μm (cw Ar^+). The clearly visible triangular distortion was observed to rotate with the mask. This intensity distortion is attributed to the measured phase distortion shown in Fig. 7(a). The simulated Bessel beam in Fig. 7(d) closely resembles this figure.

asymmetry in the first few rings, whereas little or no corresponding asymmetry is apparent in the 1-μm image. This pattern rotated with the mask and persisted if the illuminating beam was moved over the mask. Our numerical far-field simulations described above show that a low-order phase distortion in the mask substrate, or alternately a low-order geometric mask distortion, can account for this observation. In our case, the measured phase distortion in the substrate, shown in Fig. 7(a), can completely account for the observations. That is, the 0.3-λ IR peak-to-valley three-lobed phase-front distortion leads to hardly visible asymmetries in the IR [compare Figs. 2 and 7(c)], but the corresponding 0.6 λ of phase distortion in the green gives rise to the pronounced and easily detectable azimuthal intensity asymmetry seen in Figs. 8 and 7(d).

From these wavelength scaling experiments we conclude that Bessel beam masks, or any equivalent Bessel beam generating configuration,[6,7] must have low-order phase-front distortions not exceeding λ/4 (peak to valley) and high-frequency rms phase distortions of $\leq \lambda/10$ if significant asymmetric patterns, scattering loss, and speckle formation are to be avoided. Also, small-scale irregularities in the mask geometry that may result from numerical mask generation are inconsequential, whereas systematic (low-frequency) errors in the width of the annulus have to be kept at $\leq 1\%$.

An intuitive understanding of Bessel beams is obtained by thinking of a linear combination of plane waves whose wave vectors lie on a cone of opening angle θ. The x–y Fourier transform of the electric field vector of a Bessel beam is a ring; this is the same ring that generates the Bessel beam in Fig. 1. At the same time, the zero-order Bessel beam can be seen as a plane wave with a reduced wave vector $k_{\parallel} = k \cos\theta$, as in our displayed equation. The angle θ is given by an $\theta = d/2f$, where d is the ring diameter in Fig. 1. The change of sign of the E field at the zero zero crossings corresponds to a π-phase shift in those regions of the otherwise planar phase front of the Bessel beam. A numerical simulation of an interferogram and its experimental counterpart are shown in Fig. 9. The phase jumps in the regions of the J_o^2 minima are clearly seen in this figure. Furthermore, we have investigated the phase front of the center lobe of this beam with high accuracy by using spatial synchronous phase detection[14] and we have found that the phase front was planar within the interferometer resolution of λ/80 rms.

Efficient Bessel beam generation can be obtained with lasers by using an unstable resonator configuration. Such unstable resonators naturally generate ring-shaped beams, which loosely approximate the requirements for Bessel beam generation. An imaging unstable ring resonator configuration[15,16] is particularly well suited because it images an enlarged version of the scraper mirror onto itself. In practice, the sharpness of this image suffers from the finite Fresnel number of the experimental resonator. For this reason we have introduced in our experiments an additional hard aperture as close to the output as possible to reshape the output beam from its original 4.4-mm outer diameter to one of 3.5 mm; the inner diameter of 2.6 mm remained unchanged. This reconfiguration reduced the output energy by a factor of ~2. However, this Bessel beam generation efficiency of ~50% compares favorably with any of the other experimental values obtained to date. The Bessel beam was then generated with a 7.7-m focal-length lens, which permitted diffraction to fill in the center portion of the beam at the lens. The diameter of the

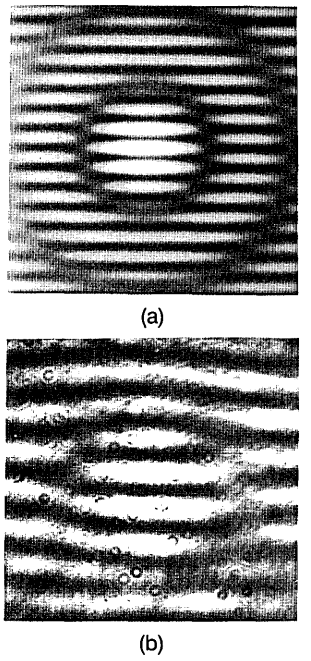

Fig. 9. Mach–Zehnder interferograms of Bessel beams: (a) numerical simulation corresponding to experimental data shown in (b). Note the clearly visible π-phase jumps when crossing the Bessel beam minima. High-accuracy interferometry of the central spot using spatial synchronous phase detection has yielded a planar phase front of ≤ λ/80 rms. The small circles in (b) are a consequence of dust inside the imaging objective.

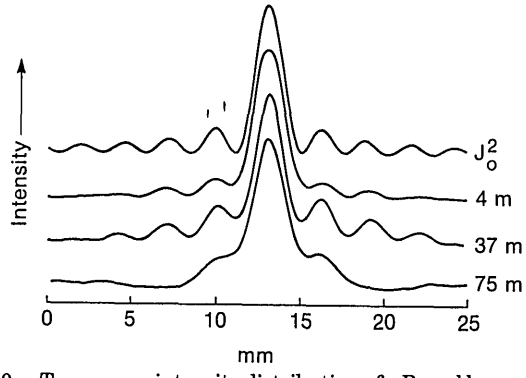

Fig. 10. Transverse-intensity distribution of a Bessel beam generated by using the ring-shaped output from an unstable ring Nd:YLF resonator. The J_o^2 distribution shown corresponds to the parameters of the experimental data. The Bessel beam generation efficiency for this setup is ~50% and could be further improved in an optimized setup.

first zero of the Bessel beam was 4 mm and remained unchanged over a distance of ~75 m (see Fig. 10). Although the central spot size was still ~4 mm, at the geometric focal range of ~100 m the Bessel beam was significantly distorted because of known phase distortions present in the output beam from the oscillator. A Gaussian beam of the same FWHM would have a depth of focus of twice the Rayleigh range, or $2z_R \approx$ 19 m. Spreading of the spot beyond that distance is significant, whereas the spot size of the Bessel beam remained unchanged over nearly five times that distance. At that distance the Gaussian beam would have opened up to a FWHM of ~21 mm.

Conclusions

The size of the central lobe of the Bessel beam as measured by the FWHM of the J_o^2 is typically smaller than either the smallest Gaussian beam or the smallest Airy disk that can be produced by the same lens. For the purpose of comparison we take a Gaussian beam with a 1/e width of its E field distribution of w_L such that $w_L \approx D_{\text{lens}/3}$, resulting in a FWHM in the focal plane of $D_{\text{Gauss}} \approx 1.13\, f\#\lambda$, where $f\#$ corresponds to the f-number of the lens. The corresponding estimate for the Airy disk is $D_{\text{Airy}} \approx 1.01\, f\#\lambda$. For the Bessel beam we choose a ring mask with a diameter equal to that of the lens for a setup as shown in Fig. 1. The FWHM is then estimated to be $D_{\text{Bessel}} \approx 0.70\, f\#\lambda$.

Whereas the FWHM of the Bessel beam is clearly the smallest of the three possibilities to generate small spot sizes with a given lens, the peak intensity is smallest for the Bessel beam. In contrast, the depth of focus, i.e., the length over which neither spot size nor peak intensity changes appreciably, is by far the largest for the Bessel beam. For the above example, we find that the peak intensity times the focal range is roughly equal for the Gaussian and the Bessel beams if we assume equal power on the lens.

For applications where depth of focus and beam definition (i.e., spot size) are of prime importance, Bessel beams present significant advantages over Gaussian beams or Airy spots. Such applications certainly encompass long-distance alignment aids or the material processing of poorly defined surfaces (machining or direct-write lithographic applications), for which laser power is not of prime concern but beam definition is. Common to most applications of Bessel beams are probably nonlinear or threshold detectors or processes.

Our present experimental and numerical investigations have shown that high-quality Bessel beam generation sets limits to permissible low-frequency phase-front errors of $\leq \lambda/4$ (peak to valley) and high-frequency errors of $\leq \lambda/10$ (rms). Geometric mask errors must be kept at $\leq 1\%$ of the ring width for low-frequency errors, whereas high-frequency (edge definition) errors may be as high as 5 to 10% of the ring width without causing deleterious effects. These limits are easily translated into requirements for other Bessel beam generation configurations.[6,7]

Our phase-front measurements of Bessel beams confirm their basic planar wave-front character, albeit with π-phase jumps between adjacent rings.

This research was partially supported by the Research Technology Corporation and the sponsors of the Laboratory for Laser Energetics. These sponsors include the Empire State Electric Energy Research Corporation, the New York State Energy Research and Development Authority, Ontario Hydro, and the University of Rochester. The authors thank T. Kessler for his help with the experiments and for numerous discussions, and R. Bahr for help with the film MTF measurements. We also acknowledge helpful discussions with C. R. Stroud.

References and Notes

1. J. Durnin, "Exact solutions for nondiffracting beams. I. The scalar theory," J. Opt. Soc. Am. A **4,** 651–654 (1987).
2. J. Durnin, J. J. Miceli, Jr., and J. H. Eberly, "Comparison of Bessel and Gaussian beams," Opt. Lett. **13,** 79–80 (1988).
3. P. Sprangle and B. Hafizi, "Critique of nondiffracting beams," Phys. Rev. Lett. **66,** 837 (1991).
4. J. Durnin, J. J. Miceli, Jr., and J. H. Eberly, "Reply to comment by Sprangle and Hafizi," Phys. Rev. Lett. **66,** 838 (1991).
5. J. Durnin, J. J. Miceli, Jr., and J. H. Eberly, "Diffraction-free beams," Phys. Rev. Lett. **58,** 1499–1501 (1987).
6. J. Turunen, A. Vasara, and A. T. Friberg, "Holographic generation of diffraction-free beams," Appl. Opt. **27,** 3959–3962 (1988).
7. G. Indebetouw, "Nondiffracting optical fields: some remarks on their analysis and synthesis," J. Opt. Soc. Am. A **6,** 150–152 (1989).
8. F. Gori, G. Guattari, and C. Padovani, "Bessel–Gauss beams," Opt. Commun. **64,** 491–495 (1987); L. Vicari, "Truncation of nondiffracting beams," Opt. Commun. **70,** 263–266 (1989); M. Zahid and M. S. Zubairy, "Directionality of partially coherent Bessel-Gauss beams," Opt. Commun. **70,** 361–364 (1989); É. A. Iolynkina, E. A. Lbragimov, and T. Usmanov, "Diffraction convergence of freely propagating beams," Sov. J. Quantum Electron. **18,** 1509–1510 (1988).
9. K. Uehara and H. Kikuchi, "Generation of nearly diffraction-free laser beams," Appl. Phys. B **48,** 125 (1989).
10. K. Thewes, M. A. Karim, and A. A. S. Awwal, "Refractive solutions for a diffraction-free beam," in *1990 Annual Meeting Digest,* Vol. 15 of OSA 1990 Technical Digest Series (Optical Society of America, Washington, D.C., 1990), paper ThRR4; "Diffraction-free beam generation using refracting systems," Opt. Laser Technol. **23,** 105 (1991).
11. D. R. MacQuigg, "Film calibration method for the analysis of laser light energy distribution," Appl. Opt. **16,** 2028 (1977).
12. A similar technique was used by S. Skupsky and T. Kessler, "A source of hot spots in frequency-tripled laser light," Opt. Commun. **70,** 123 (1989).
13. M. Born and E. Wolf, *Principles of Optics,* 4th ed. (Pergamon, Oxford, 1970), Chap. 9, p. 463. One of the reviewers drew our attention to this.
14. Laboratory for Laser Energetics, "High-power laser interferometry," in *1987 Annual Report,* Rep. DOE/DP/40200-64 (University of Rochester, Rochester, N.Y., 1987), pp. 114–123.
15. A. E. Siegman, *Lasers* (University Science Books, Mill Valley, Calif., 1986), p. 901.
16. D. Y. Park, W. Seka, Y. Lin, and D. L. Brown, "Operational characteristics of an imaging, unstable ring resonator using Nd:YLF as active medium," in *Proceedings of the International Conference on LASERS '89,* D. G. Harris and T. M. Shay, eds. (STS, McLean, Va., 1990), pp. 449–456.